Acta Materialia 298 (2025) 121404

Contents lists available at ScienceDirect

Acta Materialia

journal homepage: www.elsevier.com/locate/actamat

Full length article

A journey through the defects structure in (Nd,Tm)-doped ceria electrolytes using x-rays absorption and μ-Raman spectroscopies at cryogenic temperatures

Sara Massardo [a], Cristina Artini [b,c,*], Davide Marchelli [b], Alberto Martinelli [d], Francesco d'Acapito [e], Maria Maddalena Carnasciali [b], Marcella Pani [b,d]

[a] CNR-ICMATE, c/o DICCA-UNIGE, Via all'Opera Pia 15, 16145 Genova, Italy
[b] DCCI, Department of Chemistry and Industrial Chemistry, University of Genova, Via Dodecaneso 31, 16146 Genova, Italy
[c] CNR-ICMATE, Via De Marini 6, 16149 Genova, Italy
[d] CNR-SPIN Genova, Corso Perrone 24, 16152 Genova, Italy
[e] CNR-IOM-OGG c/o ESRF – The European Synchrotron, 71 Avenue des Martyrs CS 40220, Grenoble Cédex 9, 38043, France

ARTICLE INFO

Keywords:
Ceria
Raman spectroscopy
EXAFS
Fuel cell materials
Defects

ABSTRACT

Doping ceria with trivalent rare earth (RE) ions gives rise to systems characterized by a high ionic conductivity in the intermediate temperature range (773–973 K), making these oxides possible solid electrolytes for solid oxide cells. A combined X-ray absorption and low temperature μ-Raman spectroscopy study was performed on $Ce_{1-x}(Nd_{0.74}Tm_{0.26})_xO_{2-x/2}$ with x ranging between 0.05 and 0.60, to investigate the local structural properties of the system and to correlate them with the average ones. The origin of an extra mode occurring close to the most intense signal in the Raman spectrum of samples with $x \leq 0.30$ was explained and attributed to the effect of local collapses in the Ce-O interatomic distances, induced by the creation of vacancies. Moreover, a strong deformation of the ceria structure was observed starting from $x = 0.20$, causing a shrinkage of the Ce/RE-O and Ce/RE-Ce/RE distances within the first two coordination shells. The so obtained local scale information is of help in providing a comprehensive overview of the structural properties of rare earth doped ceria.

1. Introduction

Nowadays, the scientific community is strongly concerned with the development of new technologies for the sustainable conversion and storage of energy, as a response to the current climatic emergency. Within this framework, the research on solid oxide fuel and electrolysis cells (SOFCs and SOECs, respectively) plays a pivotal role. Among the materials employed in cells working in the intermediate temperature range (673–973 K), ceria (CeO_2) doped with trivalent rare earth (RE) elements forms a family of widely studied oxides, exhibiting remarkable values of ionic conductivity, ranging between 0.01 and 0.1 S cm^{-1} at temperatures close to 873 K [1,2]. This class of materials finds possible applications in memristive devices [3] and in gas sensors [4,5], as well as in fuel and electrolysis cells [6,7], where doped ceria acts as the electrolyte.

The mechanism of ionic conductivity in $Ce_{1-x}RE_xO_{2-x/2}$ systems implies the introduction of RE ions having a lower valence with respect to Ce^{4+}, which induces the formation of oxygen vacancies ($V_O^{\bullet\bullet}$, according to the Kröger–Vink notation [8]) for charge balance. The so obtained $V_O^{\bullet\bullet}$ are free to move across the CeO_2-based structure, especially at low doping content, through a vacancy hopping mechanism [2], thus enabling the systems to conduct O^{2-} ions. The incorporation of different RE ions into the cubic cell of ceria has been thus extensively studied with the aim to optimize the conductivity properties of the material [9–11]: among all the explored possibilities, the most effective doping ions result to be Gd^{3+} and Sm^{3+} [12].

A random replacement of Ce^{4+} by RE ions (RE'_{Ce}, again according to the *Kröger–Vink* notation [8]) occurs within the CeO_2 structure (belonging to the $Fm\bar{3}m$ space group, hereinafter labelled as F) [13] without causing significant structural distortions up to a certain doping ions content. This threshold is strictly dependent on the identity of the RE ions [10]. Based on diffraction data, the maximum x value (x_{max}) ranges for instance between ~0.20 for RE ≡ Gd^{3+} [13], ~0.30 for RE ≡

* Corresponding author.
E-mail address: artini@chimica.unige.it (C. Artini).

https://doi.org/10.1016/j.actamat.2025.121404
Received 11 March 2025; Received in revised form 1 August 2025; Accepted 5 August 2025
Available online 6 August 2025

Sm^{3+}[14], and ~0.50 for RE ≡ (Nd^{3+},Tm^{3+}) [15]. Below x_{max}, a CeO_2-based solid solution containing isolated and finely dispersed RE'_{Ce} defects is stable. When, on the contrary, the doping amount overcomes x_{max}, the F structure does not longer tolerate the insertion of doping ions, and two different scenarios can occur:

- For $RE^{3+} \equiv Tm^{3+}$-Lu^{3+}, namely when the Ce^{4+}/RE^{3+} size mismatch exceeds a certain value, a biphasic $F + C$ region forms, with C being the cubic structure belonging to the $Ia\bar{3}$ space group, [16–18] observed for the smallest RE_2O_3.
- When RE^{3+} is a rare earth ion larger than Tm^{3+}, an intergrowth between the F and the C phases takes place, giving rise to the so-called hybrid phase (H).

In the former case, C domains independently grow within the F matrix; in the latter, they coherently grow within F: this is possible since the C structure is a superstructure of F. Irrespective of these alternative paths, the compelling issue is that C domains are not conductive and are thus responsible for the conductivity drop commonly observed in doped ceria at high doping ions amount.

Despite the previous description, ionic conductivity does not reach its maximum at x_{max}, but at a much lower x, ranging between $x = 0.15$ and $x = 0.20$, namely well within the stability region of the F-based solid solution [15,19]. This evidence can be explained considering the presence of C nanodomains locally growing within the F matrix, even at $x << x_{max}$. Such defect aggregates cannot be revealed through techniques providing an average description of the crystal structure (*e.g.* x-ray diffraction), but by local techniques, such as x-ray total scattering treated by pair distribution function (PDF) [20], μ-Raman spectroscopy [14,21], x-ray absorption spectroscopy (XAS) [22], and even by high pressure x-ray diffraction [23]. Computational studies [16,24] demonstrate that C phase domains tend to grow through two fundamental building units, namely $V_O^{\bullet\bullet}RE'_{Ce}$ positively charged dimers, and $V_O^{\bullet\bullet}2RE'_{Ce}$ neutral trimers, deriving from the association of oxygen vacancies and RE ions, with the former being more stable than the latter [15,25].

The majority of fundamental studies dealing with doped ceria rely on structural studies at the average scale; just few of them make use of data deriving from XAS [22,26,27], or treat diffraction data by the PDF approach [12,20,28]. Raman spectroscopy, on the contrary, is quite a common technique in the investigation of this material, but no studies performed on doped ceria at cryogenic temperature can be retrieved in the literature.

The core of this paper is devoted to the study of the $Ce_{1-x}(Nd_{0.74}Tm_{0.26})_xO_{2-x/2}$ system ($0.05 \leq x \leq 0.60$), to evaluate its possible use as electrolyte in solid oxides cells. The system was in fact obtained by doping ceria with a mixture of a large and a small RE ion (Nd^{3+} and Tm^{3+}, respectively), so that the average ionic size reproduces the ionic radius of Sm^{3+} with C.N. 8, namely one of the most effective doping ions of ceria in terms of ionic conductivity. This work aims at unveiling the differences between local and average structural properties [15] in the system, adopting a synergistic approach toward the evaluation of data from XAS and μ-Raman spectroscopies. Measurements presented in this work were collected in cryogenic conditions. In fact, at these temperatures the quality of the spectroscopic data is significantly enhanced, and the reduced thermal motion allows for the acquisition of more detailed and better-resolved spectra with both techniques [15].

Based on this combined approach, the origin of an extra mode occurring in the Raman spectrum of samples with $x \leq 0.30$ was explained; moreover, the presence of Ce^{3+} could be excluded, and the severe deformation of the F local structure causing a general shrinkage of the Ce/RE-O and Ce/RE-Ce/RE distances within the first two coordination shells was assessed.

2. Experimental methods

2.1. Synthesis and reference characterizations

Eight samples belonging to the $Ce_{1-x}(Nd_{0.74}Tm_{0.26})_xO_{2-x/2}$ system (NdTm-doped system) with nominal $x = 0.05$, 0.10, 0.15, 0.20, 0.30, 0.40, 0.50 and 0.60, were synthesized by coprecipitation of the corresponding mixed oxalates [29]. For each of the eight samples, stoichiometric amounts of freshly milled metallic Ce (Johnson Matthey ALPHA 99.99 wt %), Nd_2O_3 (Alfa Aesar, 99.99 wt %), and Tm_2O_3 (Mateck, 99.99 wt %) were separately dissolved in HCl (13 % vol.), and then mixed. A solution of oxalic acid in large excess was then added to the previously obtained rare earths ions solution, thus causing the precipitation of the Ce,Nd,Tm-mixed oxalates. After filtering, the oxalate powders were washed with MilliQ water, dried for 12 h, and afterwards treated in air at 1373 K for four days, giving rise to the corresponding mixed oxides with the desired stoichiometries and a high crystallinity degree. According to the nominal dopants percentage with respect to the overall rare earth content, samples were respectively named NdTm_05, NdTm_10, NdTm_15, NdTm_20, NdTm_30, NdTm_40, NdTm_50 and NdTm_60.

As reported in [15], SEM-EDS analyses were performed on the samples with a Zeiss SUPRA 40 VP-30–51 scanning electron microscope. Such investigation showed that, for each sample, the experimental stoichiometry is close to the nominal one, and the particles size increases with the RE amount, and it generally ranges between 0.5 and 2 mm. In addition, a structural and electrochemical reference study was performed on the so obtained samples using x-ray diffraction, pair distribution function analysis, and electrochemical impedance spectroscopy. Structural characterizations performed using synchrotron radiation (MCX beamline, Elettra synchrotron, Trieste, IT [15], and ID22 beamline, ESRF, Grenoble, FR [30]) showed that, at the average scale, a fluorite structure is retained in samples having $x < 0.50$. Starting from $x = 0.50$, the coherent growth of the $Ia\bar{3}$ phase is observed in the samples. In particular, the weight fraction of the C phase is below 4 % in NdTm_50, and it increases to approximately 32 % in NdTm_60.

From the electrochemical point of view [15], the system shows the maximum ionic transport when $x = 0.30$, making this the most promising composition for application in solid oxides cells. Starting from such an electrochemical study, it was indirectly observed that in $Ce_{1-x}(Nd_{0.74}Tm_{0.26})_xO_{2-x/2}$, $V_O^{\bullet\bullet}2Tm'_{Ce}$ aggregates have a higher tendency to form, with respect to $V_O^{\bullet\bullet}2Nd'_{Ce}$ ones. In addition, such trimers proved to be unstable at high temperatures, as they dissociate above a certain threshold, thus improving the ionic transport in the system.

2.2. μ-Raman analyses

Powders of each sample were pressed into pellets, and analysed by means of a Renishaw System 2000 Raman imaging microscope, using a He-Ne laser (633 nm) as an excitation source. In view of the data collection process, samples were loaded in a LINKAM THMS600, a thermal cell that allows to perform measurements on pelletized specimens down to 80 K, thanks to a liquid N_2 flux. Before starting the low-temperature run, the surface of each pellet was scanned by collecting spectra on at least three different points, to assess the homogeneity of samples. Then, low-temperature spectra were collected on the point that provided the best spectra in terms of signal-to-noise ratio. After performing preliminary tests on possible thermal paths to evaluate the response of samples to different experimental conditions, spectra were collected at 298, 148, 123, 98 and 83 K, with a cooling speed of 10 K/min, and a dwell time of 10 min before recording each measurement, to allow the correct equilibration of temperature inside the cell. The temperature range was constrained by the capacity of the Dewar flask containing liquid N_2, which is specific for the THMS600 cell, and allows to perform measurements for a maximum duration of 2 h. Analyses were

carried out in the 1000 – 100 cm^{-1} spectral region, using a total magnification of 200x, and a laser power of ~4 mW. Each spectrum is the result of 4 accumulations with an exposure time of 30 s.

Low-temperature Raman spectra were collected on the samples with $x = 0.10$, 0.20, 0.30, 0.40, 0.50 and 0.60. Upon collection, spectra underwent processing, involving baseline correction through polynomial interpolation of selected points. Then, Raman signals within each spectrum were fitted using a Pseudo-Voigt function. The processing and analyses of Raman spectra were performed by the RenishawWire software (Renishaw, UK).

2.3. X-ray absorption (XAS) spectroscopy measurements

X-ray absorption (XAS) spectra of all the samples were collected at the LISA (BM08) beamline of the European Synchrotron Radiation Facility (ESRF, Grenoble, FR) [31]. Thanks to its configuration, LISA allows to perform measurements between 5 and 90 keV [32], thus enabling to collect the XAS spectra on the $Ce_{1-x}(Nd_{0.74}Tm_{0.26})_xO_{2-x/2}$ system at the energies corresponding to the K-absorption edges of the involved rare earths, namely Ce (40.4 keV), Nd (43.6 keV), and Tm (59.4 keV). XAS spectra were collected on proper amounts of sample powders, determined by the XAFSmass software [33] according to the mixed oxides stoichiometries, to obtain a suitable response. Powders were pressed into pellets together with cellulose, used as a binder. To thoroughly inspect the EXAFS (Extended X-rays Absorption Fine Structure) region of the spectra, namely the one providing information on the interatomic distances, analyses were performed up to $k = 20$ $Å^{-1}$ (being k the photoelectron's wavevector), working in transmission conditions, using a wide, not focused x-ray beam, due to the homogeneity of the pellets; during measurements, samples were kept at low temperature (80 K) using a liquid N_2 cryostat, to increase the spectral resolution.

Performing XAS measurements at high energies provides spectra characterized by quite broad absorption edges (the core-hole broadening is around 15–30 eV [34]): this prevents an in-depth analysis of the XANES (X-ray Absorption Near Edge Structure) region of the spectra, which would convey information on the oxidation state and coordination of the target atom. As a consequence, further pellets were prepared to collect XANES spectra at the LIII-absorption edges of Ce (5723 eV), Nd (6208 eV) and Tm (8648 eV). In addition, for the last-mentioned element, also the EXAFS region of the spectra was collected, up to $k = 12$ $Å^{-1}$. Analyses were performed at room temperature; data were collected in transmission for the most abundant rare earths in the samples, namely Ce and Nd, and with a 12-elements High Purity Germanium (HPGe) fluorescence detector for Tm.

Both the K- and LIII-edges spectra were collected with a silicon (311) flat crystal monochromator, which allows to work in the 4.9 – 72 keV energy range. To collect the K-edges spectra, no mirrors were involved in the optical path of x-rays; for the LIII-edges, on the other hand, Si-coated mirrors were used, to collimate and focus the x-rays beam.

The pure commercial oxides of the different rare earths were used as references and simultaneously analysed while collecting spectra of the samples at the different edges; in particular, CeO_2 (Strem Chemicals, 99.9 wt %) was used for Ce edges, Nd_2O_3 (Alfa Aesar, 99.99 wt %) for Nd edges, and Tm_2O_3 (Mateck, 99.99 wt %) for Tm edges. Moreover, an in-house synthesized sample of Ce_2O_3 was tested at the Ce LIII-edge.

For all the inspected edges, at least three spectra were collected on each sample: measurements were performed on the point characterized by the most homogeneous optical density. Spectra were then merged and elaborated, using the Demeter suite [35].

3. Results

3.1. μ-Raman investigation

Fig. 1 shows a normalized view of the Raman signals occurring in the analysed samples at room temperature. According to the literature [36],

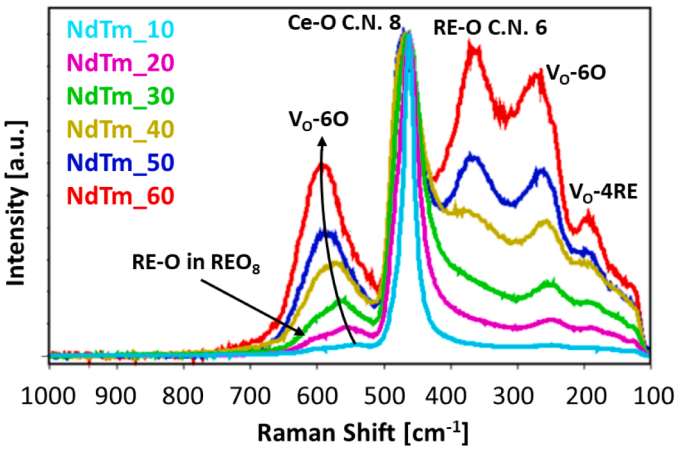

Fig. 1. Attribution of the different Raman active vibrations detectable at room temperature.

pure ceria is characterized by only one Raman active vibration, which is attributable to the triply degenerate Ce-O F_{2g} vibrational mode, located at ~ 465 cm^{-1}. In doped ceria compounds, the signal becomes asymmetric, and at 10 – 30 % percent of Ce substitution, its shape seems to point at the presence of an additional Raman signal at ~480 cm^{-1}, partially concealed by the most intense one. With increasing the RE amount, the Raman shift of Ce-O signal generally increases up to $x = 0.4$ – 0.6 [14,37,38], depending on the doping ion (*e.g.* up to $x = 0.5$ for the NdTm-doped system [15]), while its profile becomes progressively broader and less intense, due to the progressive symmetry loss taking place in the system, and to the occurrence of defects.

Simultaneously, new Raman active vibrations rise, due to the growth of defects within the fluorite-type structure; as reported in previous works [15,39], oxygen vacancies are responsible for the presence of four different Raman modes in $Ce_{1-x}(Nd_{0.74}Tm_{0.26})_xO_{2-x/2}$ system, located at ~ 250, ~ 540, ~ 190 and ~ 600 cm^{-1}. The first two signals are given by the interaction between a vacancy and the six nearest oxygen ions ($V_O^{\bullet\bullet}$ - *6O*), while the third one derives from the interaction of a vacancy with the four nearest rare earth ions ($V_O^{\bullet\bullet}$ - *4RE*). Moreover, also the signal at ~ 600 cm^{-1} is generally observed, and it is attributed to the formation of REO_8 clusters that do not contain vacancies [39]. As noticeable from the figure, the REO_8 signal at ~ 600 cm^{-1} and the $V_O^{\bullet\bullet}$ - *6O* one at ~ 540 cm^{-1} tend to overlap with increasing the RE content, becoming indistinguishable. At variance with the Ce-O F_{2g} vibrational mode, signals related to defects occurring in $Ce_{1-x}RE_xO_{2-x/2}$ systems tend to sharpen and grow in intensity with increasing the x value.

The tendency of the trivalent rare earths to coordinate six oxygen atoms is instead revealed by the appearance of a Raman signal at around 370 cm^{-1}, which is given by the occurrence of domains having the C cubic structure, typical of oxides of the smallest lanthanides; it is therefore attributed to the ($A_g + F_g$) RE-O symmetrical stretching. Such a signal is generally observed at high RE content: for the NdTm-doped system, for example, it is observed starting from $x = 0.40$.

In general, cooling a Raman-active system down to 80 K represents a valuable way to increase the resolution of its Raman spectra. Such a temperature decrease implies in fact the reduction of thermal vibrations, thus reducing the distribution width of interatomic distances, and hence the width of Raman signals. The intensity decrease of thermal vibrations also results in the need for a higher energy amount to excite a vibration, with the consequent increase in the corresponding Raman shift value.

No phase transitions were detected within the inspected temperature range. Nevertheless, at 83 K the aforementioned Raman signal at ~ 480 cm^{-1}, barely visible at room temperature, becomes evident in the Raman spectra of NdTm_10, NdTm_20 and NdTm_30. The close vicinity of this signal to the F_{2g} vibrational mode of pure ceria makes it easily attributable to a Ce-O vibration, as it is generally done in the literature [40,

41]. A comparison between the profile of the Raman spectrum of NdTm_20 in the closeness of the Ce-O vibration at room temperature (_RT) and at 80 K (_N2) is reported in Fig. 2: the extra mode in the latter is highlighted by the arrow.

The elaboration of spectra implied the fitting of the profile of each signal using a Voigt function. The description of the Ce-O signal by a single contribution was found acceptable at 298 K, but this approach proved unrealistic at lower temperatures for samples with $x \leq 0.30$, due to the presence of the abovementioned extra mode (see supplementary materials files, Figure S1). At higher *x*, on the contrary, the broadening of the most intense signal did not allow to include two contributions into the description of the Raman mode, even at the lowest temperature considered.

The temperature dependence of the Raman shift associated to the most significant vibrations was then analysed, focusing on the signals at ~ 465 cm^{-1} (related to F) and ~ 370 cm^{-1} (related to C), as well as on the one at ~ 480 cm^{-1}, namely the unattributed one. As aforementioned, all the Raman modes exhibit an increase of the Raman shift with decreasing temperature, as a consequence of the structural stiffening; this effect is visible in Fig. 3a and b. The dependence of Raman shift on composition is also interesting: Fig. 3a depicts the case of the signal at ~ 465 cm^{-1}, showing an essentially constant value for $x = 0.1$ and 0.2, and an abrupt increase up to $x = 0.5$, followed by a decrease for $x = 0.6$. This effect, already observed at room temperature in this [15] and in other [14] doped ceria systems, is the result of two competing factors, namely the introduction of an ion (or a mixture of ions) larger than Ce^{4+}, and the shrinking of the lattice due to the introduction of vacancies. The Raman shift of the extra mode, revealed for $x = 0.10$, 0.20 and 0.30, and hidden by the main signal at higher *x*, exhibits a similar trend as a function of the composition, as it presents an increasing behaviour with increasing the doping ions content, thus pointing at a strict connection between these two signals. This behaviour is even more clear at low temperature, and it can be observed in Fig. 3c, where the trends of both signals as a function of *x* at 83 K are collected.

The third thoroughly inspected Raman mode is the one related to the occurrence of the C-phase defect aggregates. This signal is located at ~374 cm^{-1} [25], and interestingly its presence becomes evident starting from $x = 0.40$, namely from a composition where the presence of the C-phase cannot be detected *via* XRD [15]. Even if data of NdTm_40 are quite scattered due to the partial covering by the broad Raman signal of the F phase, a decrease in Raman shift with increasing *x* can be clearly observed at each temperature (Fig. 4). This behaviour suggests that C defect aggregates, responsible for the appearance of the signal, mainly contain the smaller RE^{3+} ion (namely Tm^{3+}) at low *x*, and that they progressively enrich in the larger one (Nd^{3+}) with increasing *x*. This interpretation is corroborated by the comparison with room temperature spectra collected on the (Nd,Tm)- and the Sm-doped system [15],

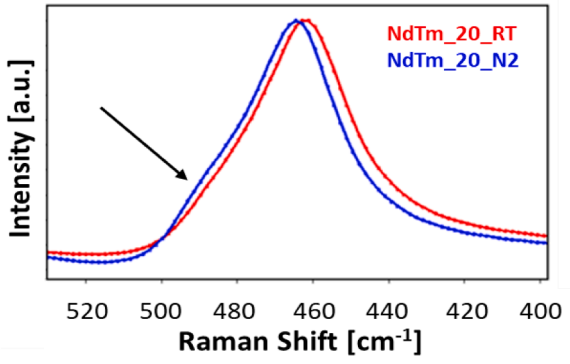

Fig. 2. Comparison between the profile of the Ce-O mode at room temperature (RT), and at the liquid nitrogen temperature (N_2). The extra signal, observed at low-temperature, is evidenced by the arrow.

which are characterized by the same average RE^{3+} size: Raman shift values of the doubly doped system are higher than the ones of Sm-doped ceria, but they tend to the latter with approaching $x = 0.6$.

3.2. XAS investigation

3.2.1. EXAFS study at 80K

The EXAFS region of XAS spectra provides information on the chemical environment around the target atom, *via* the following analytical expressions:

$$\chi(k) = \sum_{j(shells)} \frac{N_j S_0^2 f_j(k) e^{-2R_j/\lambda(k)} e^{-2k^2\sigma_j^2}}{kR_j^2} sin\left[2kR_j + \delta_j(k)\right] \quad (1)$$

$$\chi(E) = \frac{\mu - \mu_0}{\Delta\mu_0} \quad (2)$$

$$k = \frac{2\pi}{\lambda} = \sqrt{\frac{2m_e(E - E_0)}{\hbar^2}} \quad (3)$$

In Eq. (1) *f(k)* is the amplitude, S_0^2 is the amplitude attenuation factor, R_j is the interatomic distance between the target atom and the atoms belonging to the *j*-coordination shell, N_j is the coordination number, $\sigma_j^2$is the Debye-Waller factor, which accounts for the structural and thermal disorder within a shell, $\lambda(k)$ is the photoelectron mean free path, and $\delta_j(k)$ is the phase shift resulting from backscattering. In Eq. (2), μ indicates the measured linear absorption coefficient of the target atom, μ_0 is the absorption coefficient of the target as isolated atom, and $\Delta\mu_0$ is the measured jump in the absorption μ at the threshold energy E_0. In Eq. (3), m_e is the electron mass, and *E* and E_0 are the energy of the incident x-rays, and the threshold energy of the absorption edge, respectively.

A description of the radial distribution of atoms surrounding the target elements was obtained for all the samples by transforming the EXAFS function from the reciprocal (*k*-space) to the real space (*R*-space) *via* Fourier transform. Fig. 5 shows the magnitude of the Fourier transform obtained from the elaboration of EXAFS spectra collected at the K-edges on the NdTm_60 sample. In the supplementary materials files, Figure S2 shows the EXAFS spectra collected on the same sample at the different edges, together with their Fourier transform (*k*-space).

In the graph, each peak corresponds to an interatomic distance between the inspected atom and the closest ones, hence to a coordination shell: as noticeable, for all the atoms, only the first two coordination shells can be observed, and a higher disorder surrounding the atomic position occupied by Tm is suggested by the less defined shape of its peaks.

The EXAFS spectra were fitted according to the available structural models, acting on the refinable parameters in Eq. (1), namely S_0^2, R_j, and σ_j^2. The fitting process was carried out in the R-space, considering a range of interatomic distances between 1 and 4 Å, thus including up to the second coordination shell. This issue highlights the local nature of the XAS technique. The cubic F structure model of pure ceria was employed to describe the coordination shells around Ce^{4+}, while the cubic C structure of RE_2O_3 oxides (*Ia*-3 space group) was used to describe the surroundings of Nd^{3+} and Tm^{3+}. Table 1 reports the coordinates of the rare earth atoms in the structures of pure CeO_2 and RE_2O_3: according to these models, the study of the first coordination shell provides information on the Ce/RE-O distance, while the second one on the Ce/RE-Ce/RE distance. Unfortunately, the peak associated to the second coordination shell of Tm, namely the least abundant doping ion, could not be properly fitted, due to its low intensity and scarce resolution. As a consequence, no reliable information can be derived on the Tm-Ce/Nd/Tm distances.

The evolution of Ce/RE-O and Ce/RE-Ce/RE interatomic distances with varying doping amounts is depicted in Fig. 6. It can be observed that, in general, experimental errors in the determination of the

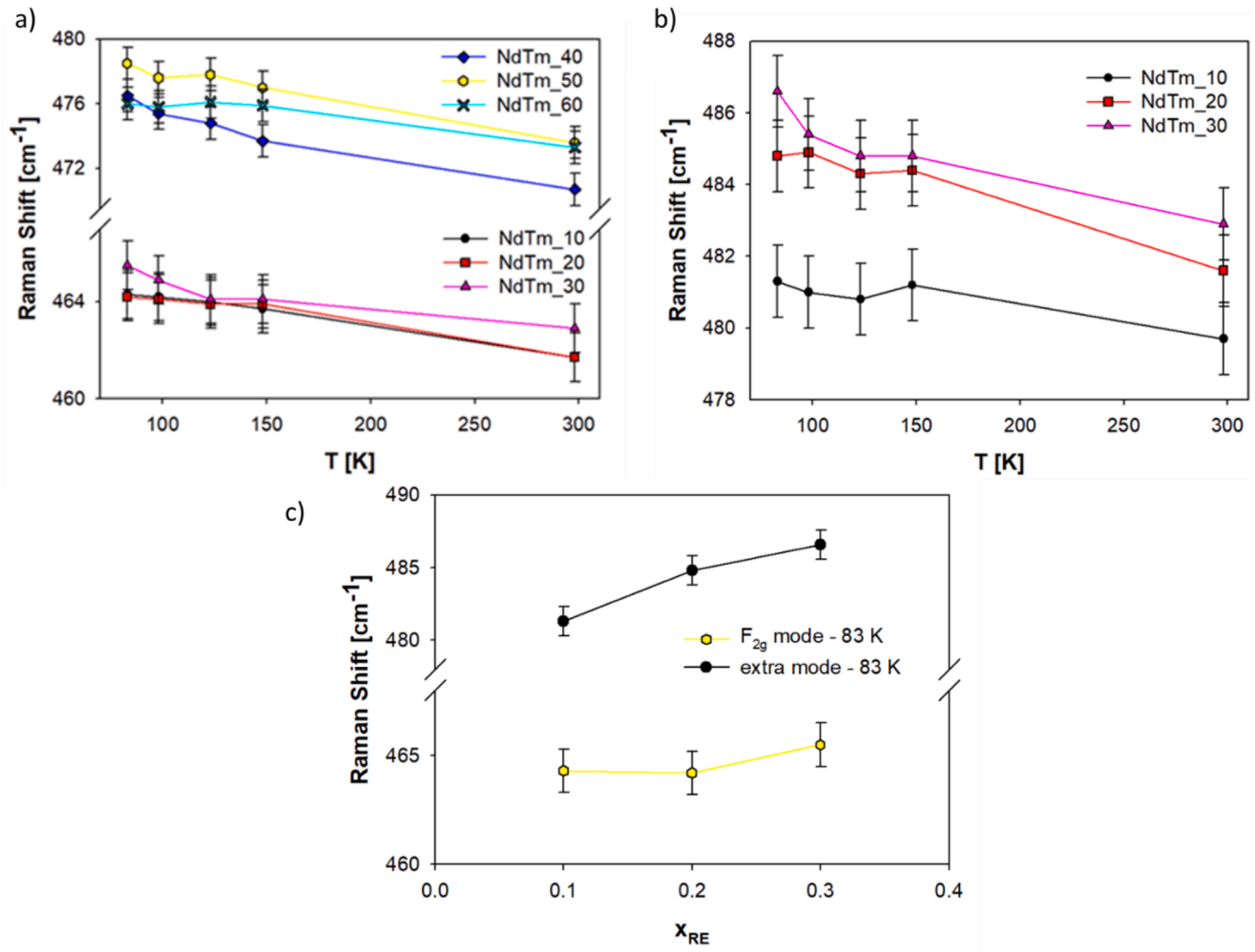

Fig. 3. Trend of the Raman shift of (a) the Ce-O vibration and (b) the extra signal as a function of temperature; (c) trend of the Raman shift of both signal *vs*. the doping ions content at 83 K.

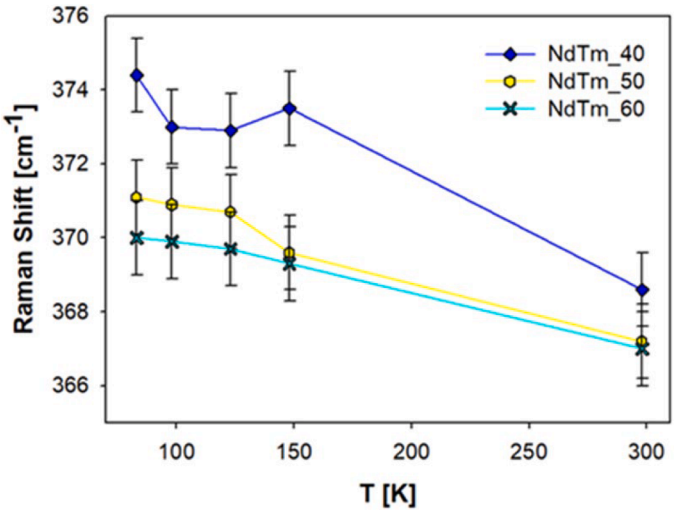

Fig. 4. Trend of the Raman shift associated to the RE-O vibration with C.N. 6, marker of the presence of C-phase domains.

interatomic distances are higher for the first shell, due to the involvement in the scattering process of oxygen, a light atom; conversely, experimental errors for the second shell, corresponding to Ce/RE-Ce/RE interatomic distances, are comparatively lower. Moreover, data also suggest that experimental errors are significantly affected by the concentration of target atoms: experimental errors on the radial distances around Ce (Fig. 6a), for instance, increase with increasing the RE content, due to the decrease in the Ce concentration, while errors on the radial distributions around Nd (Fig. 6b) tend to decrease. Finally, being Tm the least abundant element, information on the radial distribution of atoms surrounding its site is characterized by the largest uncertainty, and data appear highly scattered (Fig. 6c).

The chemical environment surrounding Ce (Fig. 6a) induces the occurrence of a roughly constant Ce-O interatomic distance up to $x = 0.20$, which closely aligns to the value observed in pure ceria (C.N. 8) in this experiment, which is 2.328 ± 0.006 Å. At $x > 0.20$, a sudden decrease in such an interatomic distance is observed, leading to ~2.27 Å for $x = 0.5$–0.6. This value is slightly lower than the one calculated *via* the Bond Valence Model [44] through the bond valence parameters provided by IUCr [45] (2013 parameters) for the Ce-O distance with C. N. 7 ($d_{Ce\text{-}O} \sim 2.28$ Å).

This evidence implies a general decrease in the coordination number around Ce^{4+}, progressively approaching a value of ~7 with increasing x beyond 0.20. Thus, starting from $x = 0.20$, the local structure around Ce^{4+} dramatically deforms, mainly due to the incorporation into the CeO_2 matrix of oxygen vacancies; the Ce-Ce/RE interatomic distance in the second coordination shell behaves analogously.

The local environment around Nd ions (Fig. 6b) also undergoes a significant distortion starting from $x = 0.20$, even if in a much more

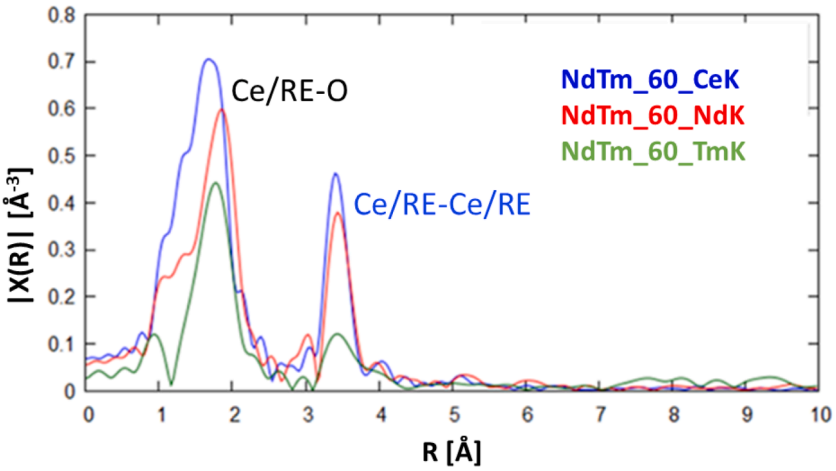

Fig. 5. Magnitude of the Fourier transform for the spectra collected on the NdTm_60 sample at the K-edges of Ce, Nd, and Tm.

Table 1
Structural models of the F and the C phase.

CeO_2 F structure *cF*12 *Fm*-3 *m* $Z = 4$			**Nd_2O_3** C structure *cI*80 *Ia*-3 $Z = 16$			**Tm_2O_3** C structure *cI*80 *Ia*-3 $Z = 16$		
$a = 5.4073(1)$ Å (ref [14].)			$a = 11.1023(2)$ Å (ref [42].)			$a = 10.4908(1)$ Å (ref [43].)		
Atom	Wyckoff position	Coordinates	Atom	Wyckoff position	Coordinates	Atom	Wyckoff position	Coordinates
Ce	4*a*	0, 0, 0	Nd1	24*d*	*x*, 0, 1/4 $x = 0.2786(3)$	Tm1	24*d*	*x*, 0, 1/4 $x = 0.2839(1)$
			Nd2	8*a*	0, 0, 0	Tm2	8*a*	0, 0, 0
O	8*c*	1/4, 1/4, 1/4	O	48*e*	*x*, *y*, *z* $x = 0.098(3)$ $y = 0.358(3)$ $z = 0.131(4)$	O	48*e*	*x*, *y*, *z* $x = 0.096(1)$ $y = 0.361(2)$ $z = 0.129(2)$
Average interatomic distances [Å]								
Ce-O 2.341(1)			Nd-O 2.40(4)			Tm-O 2.249(1)		
Ce-Ce 3.824(1)			Nd-Nd 3.71(1)			Tm-Tm 3.473(1)		

gradual way. At lower *x*, Nd-O interatomic distances remain relatively constant, pointing at a C.N. of approximately 7, value which is intermediate between the coordination at the Ce site in pure ceria (C.N. 8), and the one of Nd in pure Nd_2O_3 (C.N. 6). It is important to bear in mind that the EXAFS signal simultaneously comes from all the irradiated Nd target atoms in the sample, and it can hence be considered as a mediate response coming from all ions forming RE'_{Ce} defects in the structure, which present slightly different chemical surroundings. In this view, the intermediate value of C.N. 7 suggests that at low RE content Nd ions have a strong tendency to associate with oxygen vacancies [22], giving rise to a fluorite matrix in which RE'_{Ce} defects are dispersed, partly maintaining a C.N. 8, and partly presenting lower coordination (C.N. 6), causing local deformations in the F structure. As the doping ions amount increases, the quantity of C aggregates coherently growing within the F matrix increases, and the local environment around Nd progressively changes into the one typical of Nd_2O_3, thus implying a decrease in the Nd-O coordination toward C.N. 6. The comprehension of this result cannot disregard that the fundamental building units of the C phase are indeed formed from the association of $V_O^{\bullet\bullet}$ and RE'_{Ce}. Thus, the described evidence agrees with the interpretation of the F phase of doped ceria as a solid solution hosting oxygen vacancies at low *x*, and C-based defect aggregates at higher *x* [14].

The analysis of data collected at the Tm K-edge is much more difficult due to the high experimental errors (see Fig. 6c). Moreover, in order to increase the amount of data available at low *x*, red points, deriving from measurements performed at room temperature at the LIII-edge of Tm, were added, even if not exactly comparable to the ones obtained at 80 K at the Tm K-edge. Nevertheless, a general decrease in the coordination of the Tm first shell is appreciable, suggesting a scenario analogous to the one observed for Nd.

Overall, the behaviour observed in the Nd,Tm-doped ceria is similar to that revealed in other systems, such as Gd-doped ceria [46]. A general decrease appears, in fact, in the Nd-O (Tm-O) and Ce-O distances, more gradual for doping ions and steeper for the host atom, especially in the region where the F-C transition occurs.

3.2.2. *XANES study at room temperature*

As previously reported, XANES studies are mainly intended to determine the oxidation state and coordination of a target atom. This portion of spectra is not easy to investigate, since at variance with the EXAFS region, it cannot be described by a refinable analytical expression. Among the target atoms, the most interesting one for the purpose of this study is Ce, since it can in principle occur either as Ce^{4+} or Ce^{3+}. The issue related to the occurrence of Ce^{3+} is of importance since, if present, this ion would act as a doping ion, and its amount should not be neglected.

To evaluate the presence of Ce^{3+} in the samples, XANES spectra collected at the Ce LIII-edge on the NdTm system were compared to the ones collected on Ce^{4+} and Ce^{3+} pure oxides, used as references (see Fig. 7). By using the Athena software from the Demeter suite [35], the XANES region was described as a linear combination of CeO_2 and Ce_2O_3 XANES profiles, thus obtaining information on the relative amount of Ce^{4+} and Ce^{3+}. It emerged that the quantity of Ce^{3+} ions in each sample is lower than the limit of detection of the technique (<2 % at), thus allowing to assess that Ce in NdTm-samples is only present as a 4+ ion. Results are reported in Table S1 in the supplementary materials.

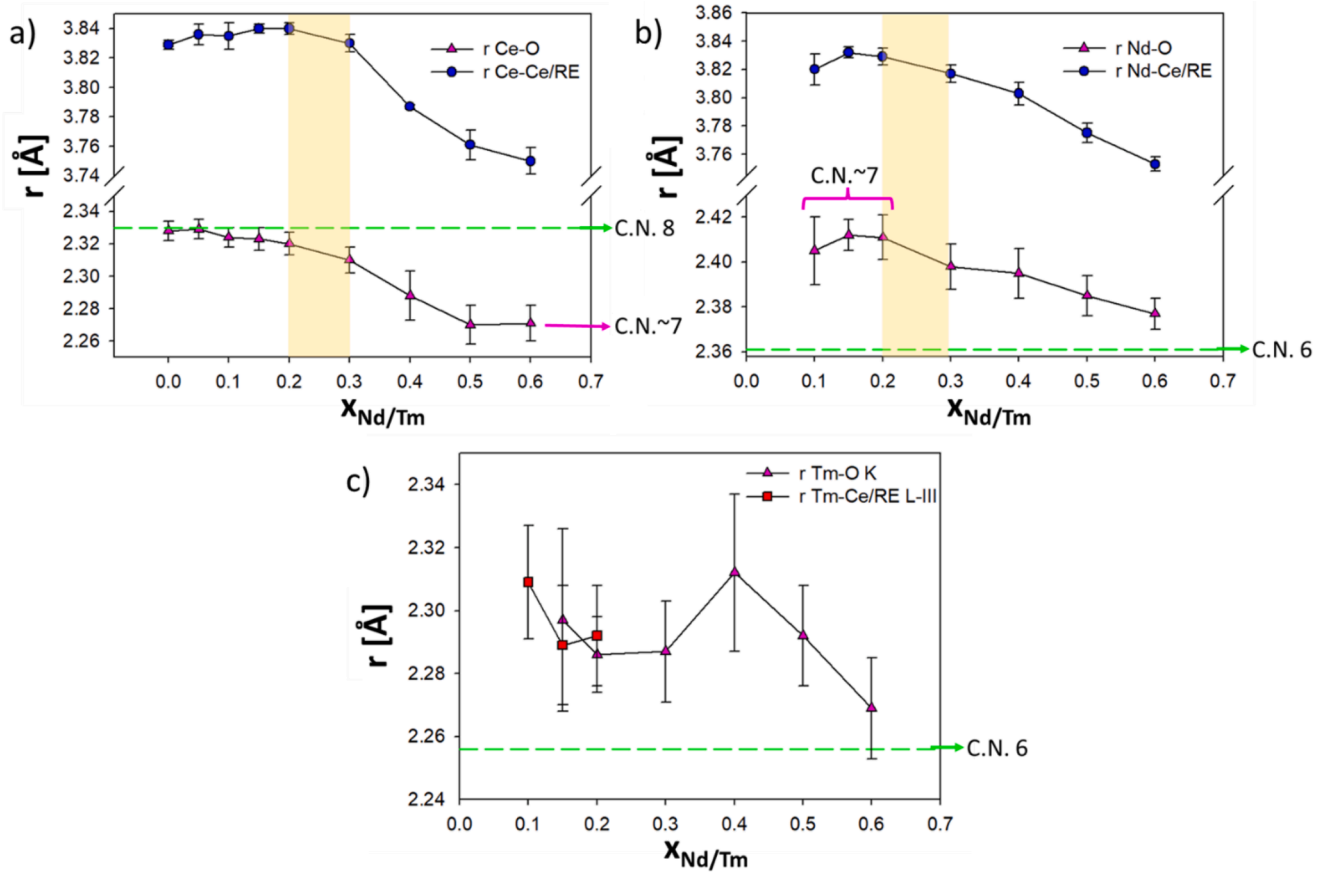

Fig. 6. Trend of the Ce/RE-O and Ce/RE-Ce/RE interatomic distances as a function of x in $Ce_{1-x}(Nd_{0.74}Tm_{0.26})_xO_{2-x/2}$ obtained from spectra collected at (a) the Ce K-edge, (b) the Nd K-edge, and (c) the Tm K- and LIII-edges.

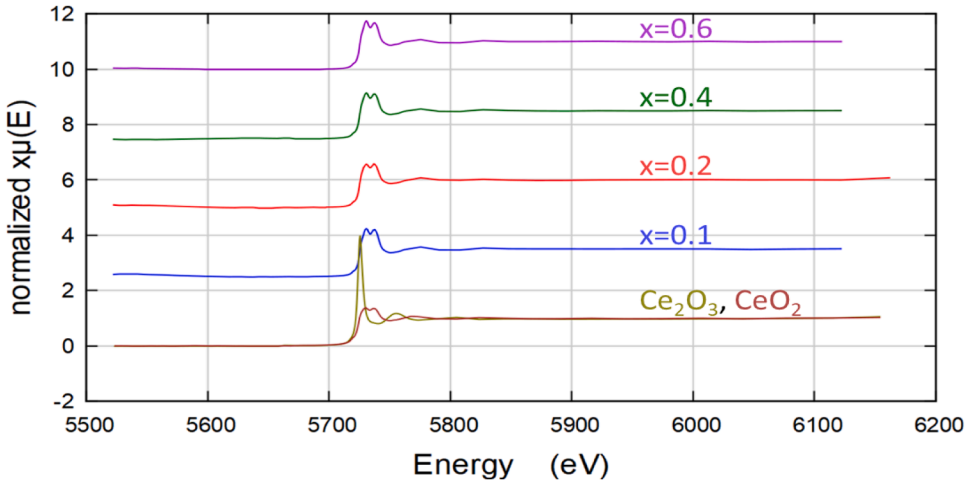

Fig. 7. Stacked view of the XANES spectra collected at the Ce LIII-edge on a selection of samples, and on CeO_2 and Ce_2O_3, used as references.

4. Discussion

Results of the μ-Raman study shed the light on one main finding: an additional Raman mode clearly appearing in the NdTm-doped samples with $x_{RE} \leq 0.30$. This extra mode is characterized by a Raman shift of approximately 480 cm^{-1}, *i.e.* very close to the one associated to the Ce-O vibration, which is the main active Raman signal for doped ceria. The latter partly hides the former at room temperature, while at temperatures as low as 80 K the extra mode emerges. Identifying the origin of such a signal is not trivial; indeed, EXAFS can be helpful.

Recalling Fig. 6, the EXAFS study suggests that a shrinkage of interatomic distances in the first and in the second shell takes place at the local scale, especially at $x > 0.20$. Such a result is also corroborated by the findings obtained on this system *via* Pair Distribution Function (PDF) at room temperature [30], and by data deriving from analogous doped ceria systems, obtained using both EXAFS [22,26] and PDF[20].

At a first glance, the local shrinkage of interatomic distances seems hardly compatible with the increase observed in the lattice parameter at the average scale *via* total scattering and x-ray diffraction experiments [15,30]. It is in fact known that the lattice parameter of doped ceria

systems increases with increasing the RE amount [1,10], due to the entrance of larger doping ions into the F matrix. Nevertheless, the decrease at the local scale finds an explanation considering the occurrence of oxygen vacancies associated to the entrance of trivalent doping ions. The F structure can be in fact described as a net of CeO_8 edge-sharing cubes [14]. When an oxygen vacancy is created by doping, *e.g.* it occupies the site highlighted in Fig. 8, the positive charges of two neighbouring Ce/RE ions are no longer shielded from each other by a bridging oxygen ion. Therefore, they tend to move away due to coulombic repulsion, thus approaching the Ce/RE ion opposite to the vacancy; at the same time, the remaining oxygen ions relax towards their adjacent vacancies: as a result, both Ce/RE–O and Ce/RE– Ce/RE distances decrease. Such an interpretation justifies the presence of shorter Ce-O interatomic distances at the local scale, which are characterized by a C.N. very close to 8 at low x, and which coexist with the longer Ce-O distances observed at the average scale. This scenario reflects into the occurrence of two distinct F_{2g} Raman active modes, which can be labelled as $F_{2g\,SR}$ (SR≡ short range) and $F_{2g\,LR}$ (LR≡ long range): the former refers to the shorter Ce-O bond, and it is hence expected at a higher Raman shift and with lower intensity than the latter, as indeed experimentally observed. Within this framework, both the primary and the extra Ce-O Raman signals stem from the same Ce-O (C.N. 8) F_{2g} vibrational modes; this interpretation also elucidates the similar behaviours observed in their Raman shifts with respect to temperature and RE content, observable in Fig. 3.

In addition, the intensity of the extra signal associated to the $F_{2g\,SR}$ increases with increasing the doping level, in agreement with the rising number of oxygen vacancies induced by doping. Interestingly, NdTm_30 exhibits the highest ionic conductivity among the studied samples [25], and correspondingly its Raman spectrum does not show the presence of any C-phase related signal. At the same time, this sample also exhibits the most pronounced extra signal, in accordance with the expected highest concentration of not-associated oxygen vacancies dissolved in the F phase. This further evidence well aligns with the described attribution of the extra mode. For $x \geq 0.40$, on the contrary, the profile of the $F_{2g\,LR}$ mode becomes so broad that it covers the $F_{2g\,SR}$ signal, thus hindering an accurate study of the behaviour of the latter.

The attribution of the extra Raman signal to the $F_{2g\,SR}$ mode holds also significant implications in terms of characterization of doped ceria. It indicates in fact that the local distortion of the Ce-O interatomic distances can be readily discerned *via* μ-Raman spectroscopy, thus without resorting to more sophisticated techniques generally used for in-depth studies of local geometries, such as PDF and XAS.

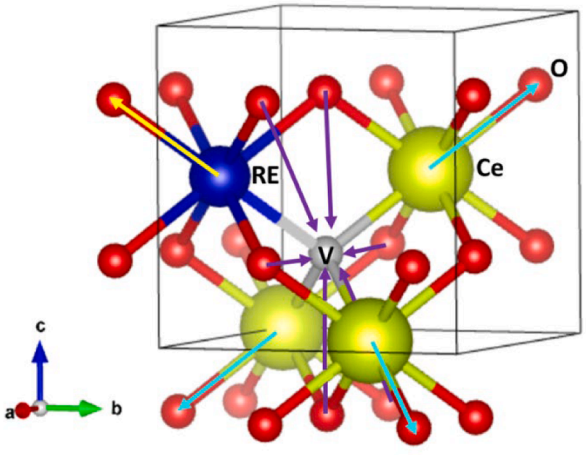

Fig. 8. An eighth of the CeO_2 cell is represented; oxygen ions are reported in red, Ce in green, and doping ions in blue. The central grey site represents a vacancy. Arrows indicate the relative displacements of different ions around a vacancy.

The above discussed interpretation is further corroborated by the exclusion of other possible reasons which could justify the appearance of the extra mode, such as the presence of a tetragonal derivative of the F phase, or the occurrence of a secondary cubic F phase.

According to Sediva et al. [47], for instance, the F structure of ceria can experience a local deformation of its cubic structure into a tetragonal one when subjected to localized stresses (*e.g.*, epitaxial growth, thin films deposition). This deformation results in the splitting of the Ce-O triply degenerate F_{2g} Raman mode into a B_{2g} singlet and an E_g doublet, being the former characterized by a Raman shift close to the one of undistorted ceria, and the latter by a slightly higher value. Such a scenario is at least in principle compatible with the one observed in bulk samples: a previous study highlighted in fact in NdTm-doped samples an increase of microstrain with increasing the doping ions amount [15], identifying this effect as a consequence of the chemical pressure induced by doping. Nevertheless, again according to Sediva et al. [47], the tetragonal deformation is expected to cause, with increasing strain, a red-shift and a blue-shift of the B_{2g} and E_g Raman modes, namely the opposite of the effect observed in Fig. 3c.

The occurrence of a tetragonal cell can be also excluded by properly treating EXAFS data. Such a distortion should in fact give rise to two distinct Ce-O (1st shell) and Ce/RE-Ce/RE (2nd shell) interatomic distances. Following this idea, the fit of the first two coordination shells was attempted both by considering the existence of two Ce-O distances in the first coordination shell (C.N. 8), also to investigate the possible occurrence of a secondary F phase, and by considering the existence of two distinct Ce/RE-Ce/RE distances in the second coordination shell (C.N. 12). In the former case, high Debye-Waller factors were obtained ($\sigma^2 > 0.01$), thus indicating the impossibility to firmly determine the atomic positions in the secondary Ce-O shell. In the latter case, reasonable Debye-Waller factors were achieved; however, the fits exhibited high R-values. To evaluate the significance of the results derived from this structural model, a χ^2-test was performed, based on the comparison between the actual fit and the one derived from the undistorted CeO_2 structure: no significant differences between the two-shell and single-shell configurations were revealed. Furthermore, the deformed model became increasingly unrealistic as the RE content in the samples increased. These findings effectively ruled out the occurrence of a tetragonal deformation in the NdTm samples and excluded the potential presence of a small amount of a secondary F phase.

Relying on the results of the EXAFS investigation, a few additional remarks can be made on the behaviour of RE doping ions.

The study performed at the rare earths K-edges showed that, for $x \leq 0.20$, the distortion around Ce atoms caused by the Nd/Tm doping is minimal, but indeed existing, and the coordination observed for Ce is close to C.N. 8, and it slowly decreases. Moreover, at this stage it has to be remarked that the possible bimodal distribution observed in the Y- and Sm-doped system by Kraynis et al. [48] by modelling EXAFS data through the reverse Monte-Carlo method cannot be *a priori* excluded. In the same compositional region, conversely, a lower C.N. of ~7 is observed for the RE-O shell: this scenario confirms the tendency of oxygen vacancies to associate with doping ions rather than with Ce^{4+}, so promoting the growth of the C phase fundamental building units, which derive from the association of $V_O^{\bullet\bullet}$ and RE'_{Ce}. In particular, a C.N. (RE-O) of 7 in the F structure implies that Nd'_{Ce} and Tm'_{Ce} doping ions tend to create aggregates where one oxygen vacancy is surrounded by two doping ions, hence allowing to observe the growth of $V_O^{\bullet\bullet}$-$2RE'_{Ce}$ neutral trimers [24]. This peculiar defect architecture was already indirectly observed in the present system *via* electrochemical impedance spectroscopy [15]. The good agreement on the nature of structural defects coming from studies performed with such different techniques is particularly encouraging, as it supports the validity and consistency of the proposed interpretation. This evidence is particularly clear for Nd, since spectra collected at the Nd K-edge are of very high quality, and experimental errors on the determination of Nd-O distances are low even at small RE content. However, given that the binding energy of

$V_O^{\bullet\bullet}$-2RE'$_{Ce}$ aggregates is higher for smaller ions [24], such a scenario seems even more realistic for Tm ions, though, in this case, experimental errors in the determination of Tm-O distances are larger, due to the very small amount of Tm in the samples. As already demonstrated [25], $V_O^{\bullet\bullet}$-2RE'$_{Ce}$ aggregates tend to dissociate above 770 K, thus increasing the performances of the electrolyte at high temperature, but they are indeed stable at low temperature. At higher x, the RE-O coordination furtherly decreases, slowly approaching the value of 6, typical of pure RE_2O_3 oxides; the intermediate C.N. (RE-O) of 6.5 describes a scenario where an oxygen vacancy is surrounded by 2–3 RE ions. Such a high RE content also implies a deformation of the F local structure around Ce^{4+}, which hence reduces the Ce C.N. toward a value of 7, thus indicating an association rate of oxygen vacancies with Ce^{4+} lower than with doping ions, but not negligible. Deguchi et al. [22] proposed an accurate EXAFS study on three different ceria systems singly doped with RE ≡ Gd, Y, and La, and x ranging between 0.05 and 0.30. Leaving aside La, which tends to form aggregates with the hexagonal structure typical of La_2O_3, they observed that the tendency of doping ions to associate with vacancies reflects the order $Gd^{3+} < Y^{3+}$, in good agreement with the lower ionic size of the latter. In the inspected compositional range, the Y^{3+} C.N. is in fact approximately 6.5 and quite stable, and the one of Gd^{3+} progressively decreases from ~7.7 to ~6.7 with increasing the Gd content. These findings highlight the higher tendency of the smallest doping ion, namely Y^{3+}, to associate with vacancies. Such a result is in good agreement with the behaviour observed in the NdTm-samples by the combined results of x-ray diffraction and impedance spectroscopy, which show the stronger tendency of Tm^{3+}, namely of the smaller ion, to associate with vacancies.

5. Conclusions

A thorough spectroscopic study of the $Ce_{1-x}(Nd_{0.74}Tm_{0.26})_xO_{2-x/2}$ system was performed by μ-Raman and x-rays absorption spectroscopies, focusing on samples with $0.05 \leq x \leq 0.60$. The main results can be summarized as follows:

- μ-Raman measurements suggest that no structural transitions occur down to 83 K. The occurrence of an extra-signal with a Raman shift of 480 cm-1 was observed for samples with $x \leq 0.30$ and ascribed to the local collapse in the Ce-O interatomic distances, induced by the creation of vacancies; this interpretation aligns well with results from XAS spectroscopy.
- The XANES study performed at room temperature at the LIII-edges of the rare earths showed the presence of the sole Ce(IV).
- The EXAFS study performed at the K-edges of the rare earths elucidated the tendency of Nd and Tm doping ions to associate with oxygen vacancies, mainly giving rise to the formation of $V_O^{\bullet\bullet}$-2RE'$_{Ce}$ clusters. In addition, a severe deformation of the F structure was observed starting from $x = 0.20$, implying the general shrinkage of the Ce/RE-O and Ce/RE-Ce/RE distances within the first two coordination shells.

Understanding how RE'$_{Ce}$ defects are associating $V_O^{\bullet\bullet}$ in these systems is of paramount importance, since aggregates formation directly affects the ionic transport properties of doped ceria electrolytes. In this experiment, the synergistic use of EXAFS and μ-Raman spectroscopy exhaustively revealed the occurrence of defect clusters.

CRediT authorship contribution statement

Sara Massardo: Writing – review & editing, Writing – original draft, Visualization, Investigation, Formal analysis, Conceptualization. **Cristina Artini:** Writing – review & editing, Writing – original draft, Visualization, Funding acquisition, Formal analysis. **Davide Marchelli:** Writing – review & editing, Investigation, Formal analysis. **Alberto Martinelli:** Writing – review & editing, Investigation. **Francesco d'Acapito:** Writing – review & editing, Supervision, Conceptualization. **Maria Maddalena Carnasciali:** Writing – review & editing, Supervision, Conceptualization. **Marcella Pani:** Writing – review & editing, Supervision, Resources, Funding acquisition, Formal analysis.

Declaration of competing interest

The authors declare that they have no known competing financial interests or personal relationships that could have appeared to influence the work reported in this paper.

Supplementary materials

Supplementary material associated with this article can be found, in the online version, at doi:10.1016/j.actamat.2025.121404.

References

[1] M. Mogensen, Physical, chemical and electrochemical properties of pure and doped ceria, Solid State Ion. 129 (1–4) (2000) 63–94, https://doi.org/10.1016/S0167-2738(99)00318-5.

[2] H. Inaba, Ceria-based solid electrolytes, Solid State Ion. 83 (1–2) (1996) 1–16, https://doi.org/10.1016/0167-2738(95)00229-4.

[3] J.J. Yang, D.B. Strukov, D.R. Stewart, Memristive devices for computing, Nat. Nanotechnol. 8 (1) (2013) 13–24, https://doi.org/10.1038/nnano.2012.240.

[4] J. Gerblinger, W. Lohwasser, U. Lampe, H. Meixner, High temperature oxygen sensor based on sputtered cerium oxide, Sens. Actuators B Chem. 26 (1–3) (1995) 93–96, https://doi.org/10.1016/0925-4005(94)01564-X.

[5] H.-J. Beie, A. Gnörich, Oxygen gas sensors based on CeO_2 thick and thin films, Sens. Actuators B Chem. 4 (3–4) (1991) 393–399, https://doi.org/10.1016/0925-4005(91)80141-6.

[6] L. Spiridigliozzi, E. Di Bartolomeo, G. Dell'Agli, F. Zurlo, GDC-based infiltrated electrodes for solid oxide electrolyzer cells (SOECs), Appl. Sci. 10 (11) (2020) 3882, https://doi.org/10.3390/app10113882.

[7] A. Nechache, S. Hody, Alternative and innovative solid oxide electrolysis cell materials: a short review, Renew. Sustain. Energy Rev. 149 (2021) 111322, https://doi.org/10.1016/j.rser.2021.111322.

[8] Kröger, F.A.; Vink, H.J. Relations between the concentrations of imperfections in crystalline solids; 1956; pp 307–435. https://doi.org/10.1016/S0081-1947(08)60135-6.

[9] R. Schmitt, A. Nenning, O. Kraynis, R. Korobko, A.I. Frenkel, I. Lubomirsky, S. M. Haile, J.L.M. Rupp, A review of defect structure and chemistry in Ceria and its solid solutions, Chem. Soc. Rev. 49 (2) (2020) 554–592, https://doi.org/10.1039/C9CS00588A.

[10] C. Artini, Rare-earth-doped ceria systems and their performance as solid electrolytes: a puzzling tangle of structural issues at the average and local scale, Inorg. Chem. 57 (21) (2018) 13047–13062, https://doi.org/10.1021/acs.inorgchem.8b02131.

[11] M. Balaguer, C. Solís, J.M. Serra, Structural–transport properties relationships on $Ce_{1-x}Ln_xO_{2-\delta}$ system (Ln = Gd, La, Tb, Pr, Eu, Er, Yb, Nd) and effect of cobalt addition, J. Phys. Chem. C 116 (14) (2012) 7975–7982, https://doi.org/10.1021/jp211594d.

[12] M. Coduri, S. Checchia, M. Longhi, D. Ceresoli, M. Scavini, Rare earth doped ceria: the complex connection between structure and properties, Front. Chem. (2018) 6, https://doi.org/10.3389/fchem.2018.00526.

[13] C. Artini, G.A. Costa, M. Pani, A. Lausi, J. Plaisier, Structural characterization of the CeO_2/Gd_2O_3 mixed system by synchrotron X-ray diffraction, J. Solid State Chem. 190 (2012) 24–28, https://doi.org/10.1016/j.jssc.2012.01.056.

[14] C. Artini, M. Pani, M.M. Carnasciali, M.T. Buscaglia, J.R. Plaisier, G.A. Costa, Structural features of Sm- and Gd-doped ceria studied by synchrotron X-ray diffraction and μ-raman spectroscopy, Inorg. Chem. 54 (8) (2015) 4126–4137, https://doi.org/10.1021/acs.inorgchem.5b00395.

[15] C. Artini, S. Presto, M. Viviani, S. Massardo, M.M. Carnasciali, L. Gigli, M. Pani, The role of defects association in structural and transport properties of the $Ce_{1-x}(Nd_{0.74}Tm_{0.26})_xO_{2-x/2}$ system, J. Energy Chem. 60 (2021) 494–502, https://doi.org/10.1016/J.JECHEM.2020.11.030.

[16] Z.-P. Li, T. Mori, J. Zou, J. Drennan, Defects clustering and ordering in di- and trivalently doped ceria, Mater. Res. Bull. 48 (2) (2013) 807–812, https://doi.org/10.1016/j.materresbull.2012.11.073.

[17] F. Ye, T. Mori, D.R. Ou, J. Zou, G. Auchterlonie, J. Drennan, Compositional and structural characteristics of nano-sized domains in gadolinium-doped ceria, Solid State Ion. 179 (21–26) (2008) 827–831, https://doi.org/10.1016/j.ssi.2008.02.034.

[18] Z.-P. Li, T. Mori, F. Ye, D.R. Ou, J. Zou, J. Drennan, Structural phase transformation through defect cluster growth in Gd-doped ceria, Phys. Rev. B 84 (18) (2011) 180201, https://doi.org/10.1103/PhysRevB.84.180201.

[19] S. Presto, C. Artini, M. Pani, M.M. Carnasciali, S. Massardo, M. Viviani, Ionic conductivity and local structural features in $Ce_{1-x}Sm_xO_{2-x/2}$, Phys. Chem. Chem. Phys. 20 (44) (2018) 28338–28345, https://doi.org/10.1039/C8CP04186E.

[20] M. Scavini, M. Coduri, M. Allieta, M. Brunelli, C. Ferrero, Probing complex disorder in $Ce_{1-x}Gd_xO_{2-x/2}$ using the pair distribution function analysis, Chem. Mater. 24 (7) (2012) 1338–1345, https://doi.org/10.1021/cm203819u.
[21] C. Artini, S. Presto, S. Massardo, M. Pani, M.M. Carnasciali, M. Viviani, Transport properties and high temperature Raman features of heavily Gd-doped ceria, Energ. (Basel) 12 (21) (2019), https://doi.org/10.3390/en12214148.
[22] H. Deguchi, H. Yoshida, T. Inagaki, M. Horiuchi, EXAFS study of doped ceria using multiple data set fit, Solid State Ion. 176 (23–24) (2005) 1817–1825, https://doi.org/10.1016/j.ssi.2005.04.043.
[23] C. Artini, S. Massardo, M.M. Carnasciali, B. Joseph, M. Pani, Evaluation of the defect cluster content in singly and doubly doped ceria through *in situ* high-pressure X-ray diffraction, Inorg. Chem. (10) (2021) 60, https://doi.org/10.1021/acs.inorgchem.1c00433.
[24] L. Minervini, Defect cluster formation in M_2O_3-doped CeO_2, Solid State Ion. 116 (3–4) (1999) 339–349, https://doi.org/10.1016/S0167-2738(98)00359-2.
[25] S. Massardo, M. Pani, M.M. Carnasciali, S. Presto, M. Viviani, C. Artini, Defect chemistry of (Nd,Tm)- and (Nd,Dy)-doped ceria as revealed by Raman and electrochemical impedance spectroscopy, Solid State Ion. 403 (2023) 116403, https://doi.org/10.1016/j.ssi.2023.116403.
[26] T. Ohashi, S. Yamazaki, T. Tokunaga, Y. Arita, T. Matsui, T. Harami, K. Kobayashi, EXAFS study of $Ce_{1-x}Gd_xO_{2-x/2}$, Solid State Ion. 113–115 (1998) 559–564, https://doi.org/10.1016/S0167-2738(98)00322-1.
[27] S. Yamazaki, EXAFS study of reduced ceria doped with lanthanide oxides, Solid State Ion. 154–155 (2002) 113–118, https://doi.org/10.1016/S0167-2738(02)00471-X.
[28] M. Coduri, M. Scavini, M. Pani, M.M. Carnasciali, H. Klein, C. Artini, From nano to microcrystals: effects of different synthetic pathways on the defect architecture in heavily Gd-doped ceria, Phys. Chem. Chem. Phys. 19 (18) (2017) 11612–11630, https://doi.org/10.1039/C6CP08173H.
[29] C. Artini, G.A. Costa, R. Masini, Study of the formation temperature of mixed $LaREO_3$ (RE ≡ Dy, Ho, Er, Tm, Yb, Lu) and $NdGdO_3$ oxides, J. Therm. Anal. Calorim. 103 (1) (2011) 17–21, https://doi.org/10.1007/s10973-010-0973-8.
[30] A. Martinelli, S. Massardo, C. Artini, M.M. Carnasciali, M. Pani, Unveiling the local structure of doubly doped CeO_2: a synchrotron X-ray pair distribution function study, J. Mater. Chem. Mater. 12 (13) (2024) 7788–7798, https://doi.org/10.1039/D3TA07027A.
[31] A. Martinelli, S. Massardo, An in-depth study of the defects architecture in $Ce_{(1-x)}(Nd_{0.74}Tm_{0.26})xO_{2-x/2}$ through EXAFS measurements. European synchrotron radiation facility [data set]. https://doi.org/10.15151/ESRF-ES-928798247.
[32] F. d'Acapito, G.O. Lepore, A. Puri, A. Laloni, F. La Manna, E. Dettona, A. De Luisa, A. Martin, The LISA beamline at ESRF, J. Synchrotron. Radiat. 26 (2) (2019) 551–558, https://doi.org/10.1107/S160057751801843X.
[33] Klementiev, K. XAFSmass. (www.cells.es/Beamlines/CLAESS/software/xafsmass.html).(accessed 2023-03-02).
[34] M.O. Krause, J.H. Oliver, Natural widths of atomic K and L levels, kα X-ray lines and several KLL auger lines, J. Phys. Chem. Ref. Data 8 (2) (1979) 329–338, https://doi.org/10.1063/1.555595.
[35] B. Ravel, M. Newville, ATHENA, ARTEMIS, HEPHAESTUS: data analysis for X-ray absorption spectroscopy using IFEFFIT, J. Synchrotron. Radiat. 12 (4) (2005) 537–541, https://doi.org/10.1107/S0909049505012719.
[36] W.H. Weber, K.C. Hass, J.R. McBride, Raman study of CeO_2: second-order scattering, lattice dynamics, and particle-size effects, Phys. Rev. B 48 (1) (1993) 178–185, https://doi.org/10.1103/PhysRevB.48.178.
[37] C. Artini, M. Pani, M.M. Carnasciali, J.R. Plaisier, G.A.Lu-, Sm- Costa, Gd-Doped Ceria, A comparative approach to their structural properties, Inorg. Chem. 55 (20) (2016) 10567–10579, https://doi.org/10.1021/acs.inorgchem.6b01806.
[38] C. Artini, M. Viviani, S. Presto, S. Massardo, M.M. Carnasciali, L. Gigli, M. Pani, Correlations between structure, microstructure and ionic conductivity in (Gd,Sm)-doped ceria, Phys. Chem. Chem. Phys. 24 (38) (2022) 23622–23633, https://doi.org/10.1039/d2cp03255d.
[39] A. Nakajima, A. Yoshihara, M. Ishigame, Defect-induced Raman spectra in doped CeO_2, Phys. Rev. B 50 (18) (1994) 13297–13307, https://doi.org/10.1103/PhysRevB.50.13297.
[40] D. Mukherjee, B.G. Rao, B.M. Reddy, Characterization of ceria-based nano-oxide catalysts by Raman spectroscopy, Top. Catal. 60 (19–20) (2017) 1673–1681, https://doi.org/10.1007/s11244-017-0846-5.
[41] S.Raman Loridant, Spectroscopy as a powerful tool to characterize ceria-based catalysts, Catal. Today 373 (2021) 98–111, https://doi.org/10.1016/j.cattod.2020.03.044.
[42] C. Artini, M. Pani, J.R. Plaisier, G.A. Costa, Structural study of Nd oxidation by means of in-situ synchrotron X-ray diffraction ($400 \leq T \leq 700$°C), Solid State Ion. 257 (2014) 38–41, https://doi.org/10.1016/j.ssi.2014.01.034.
[43] J. Blanusa, M. Mitric, D. Rodic, A. Szytula, M. Slaski, An X-ray diffraction and magnetic susceptibility study of $Tm_xY_{2-x}O_3$, J. Magn. Magn. Mater. 213 (1–2) (2000) 75–81, https://doi.org/10.1016/S0304-8853(99)00797-0.
[44] D.I. Brown, The Chemical Bond in Inorganic Chemistry: The Bond Valence Model, Oxford University Press, 2002, https://doi.org/10.1021/ja025226b.
[45] *https://www.iucr.org/resources/data/datasets/bond-valence-parameters*.
[46] A. Kossoy, Q. Wang, R. Korobko, V. Grover, Y. Feldman, E. Wachtel, A.K. Tyagi, A. I. Frenkel, I. Lubomirsky, Evolution of the local structure at the phase transition in CeO_2-Gd_2O_3 solid solutions, Phys. Rev. B 87 (5) (2013) 054101, https://doi.org/10.1103/PhysRevB.87.054101.
[47] E. Sediva, D. Bohdanov, G.F. Harrington, I. Rafalovskyi, J. Drahokoupil, F. Borodavka, P. Marton, J. Hlinka, Anisotropic strain in rare-earth substituted ceria thin films probed by polarized raman spectroscopy and first-principles calculations, ACS Appl. Mater. Interfaces 12 (50) (2020) 56251–56259, https://doi.org/10.1021/acsami.0c14249.
[48] O. Kraynis, J. Timoshenko, J. Huang, H. Singh, E. Wachtel, A.I. Frenkel, I. Lubomirsky, Modeling strain distribution at the atomic level in doped Ceria films with extended X-ray absorption fine structure spectroscopy, Inorg. Chem. 58 (11) (2019) 7527–7536, https://doi.org/10.1021/acs.inorgchem.9b00730.